Reduced Graphene Oxide Heterostructured Silver Nanoparticles Significantly Enhanced Thermal Conductivities in Hot-Pressed Electrospun Polyimide Nanocomposites

Yongqiang Guo,[†] Xutong Yang,[†] Kunpeng Ruan,[†] Jie Kong,[†] Mengyao Dong,[§,∥] Jiaoxia Zhang,[§,⊥] Junwei Gu,*,[†,‡] and Zhanhu Guo*,[§]

[†]MOE Key Laboratory of Material Physics and Chemistry under Extraordinary Conditions, Shaanxi Key Laboratory of Macromolecular Science and Technology, Department of Applied Chemistry, School of Science, Northwestern Polytechnical University, Xi'an, Shaanxi 710072, P. R. China

[‡]State Key Laboratory of Solid Lubrication, Lanzhou Institute of Chemical Physics, Chinese Academy of Sciences, Lanzhou 730000, P. R. China

[§]Integrated Composites Laboratory (ICL), Department of Chemical & Biomolecular Engineering, University of Tennessee, Knoxville, Tennessee 37996, United States

[∥]Key Laboratory of Materials Processing and Mold (Zhengzhou University), Ministry of Education, National Engineering Research Center for Advanced Polymer Processing Technology, Zhengzhou University, Zhengzhou 450002, P. R. China

[⊥]School of Materials Science and Engineering, Jiangsu University of Science and Technology, Zhenjiang 212003, P. R. China

Ⓢ Supporting Information

ABSTRACT: Graphene presents an extremely ultra-high thermal conductivity, well above other known thermally conductive fillers. However, graphene tends to aggregate easily due to its strong intermolecular $\pi-\pi$ interaction, resulting in poor dispersion in the polymer matrix. In this study, silver nanoparticles anchored reduced graphene oxide (Ag/rGO) were first prepared using one-pot synchronous reduction of Ag^+ and GO solution via glucose. The thermally conductive (Ag/rGO)/polyimide ((Ag/rGO)/PI) nanocomposites were then obtained via electrospinning the in situ polymerized (Ag/rGO)/polyamide electrospun suspension followed by a hot-press technique. The thermal conductivity

(λ), glass transition temperature (T_g), and heat resistance index (T_{HRI}) of the (Ag/rGO)/PI nanocomposites all increased with increasing the loading of Ag/rGO fillers. When the mass fraction of Ag/rGO (the weight ratio of rGO to Ag was 4:1) fillers was 15%, the corresponding (Ag/rGO)/PI nanocomposites showed a maximum λ of 2.12 W/(m K). The corresponding T_g and T_{HRI} values were also enhanced to 216.1 and 298.6 °C, respectively. Furthermore, thermal conductivities calculated by our established improved thermal conduction model were relatively closer to the experimental results than the results obtained from other classical models.

KEYWORDS: Ag/reduced graphene oxide (Ag/rGO), electrospinning, thermal conductivity, polyimide nanocomposites, thermal conduction model
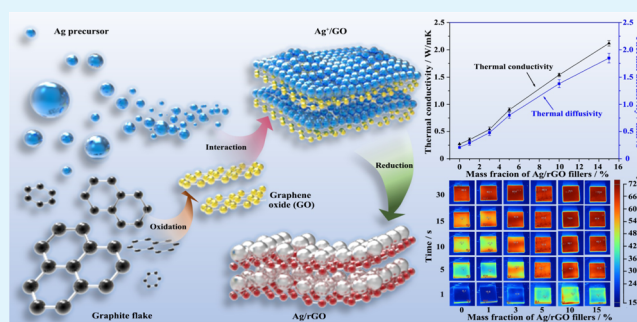
1. INTRODUCTION

Over the years, significant progress has been made toward developing electronics and energy units such as light-emitting diodes (LEDs), energy storage materials, organic solar cells, etc. to satisfy their increasingly higher requirements.[1−6] However, quick heat accumulation but slow heat dissipation become major issues.[7−9] For example, in the electronic fields, the International Technology Roadmap for Semiconductors (ITRS) predicted that the size of electronic devices would be 10 nm or less till 2020, and the generated heat from these high-performance chips would be sharply increased.[10]

Recently, thermal conductivity has been investigated extensively for polymer materials due to urgent requirements of quick and effective heat dissipation, low thermal expansion, anticorrosion, lightweight, etc.[11,12] However, polymers generally possess an intrinsic thermal conductivity (λ) less than 0.50 W/(m K), much lower than that of ceramic or metallic materials.[13] To improve the final λ values of polymers, an effective and economical method is to introduce highly thermally conductive
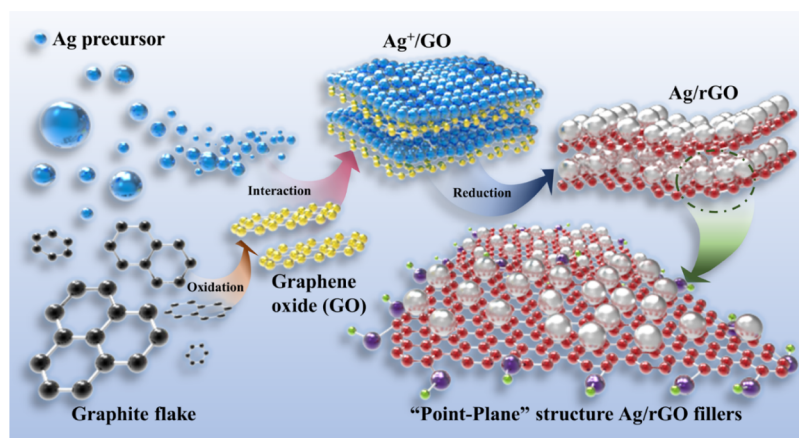
Figure 1. Schematic diagram of the fabrication of Ag/rGO fillers.

fillers to form composites.[14,15] In recent years, single and/or hybrid ceramics (such as boron nitride (BN),[16] aluminum nitride (AlN),[17] silicon carbide (SiC),[18] etc.) and metals (such as copper (Cu),[19] silver (Ag),[20] aluminum (Al),[21] etc.) have served as fillers to enhance the λ values of polymers. Carbon species (such as graphite,[22] carbon nanotubes (CNTs),[23] graphene,[24] etc.) with relatively higher λ values are the most widely employed fillers to obtain thermally conductive polymer composites. However, excessively high loading of thermally conductive fillers is commonly demanded to achieve relatively high λ values, causing significant challenges such as poor processing, deteriorated mechanical properties, higher density, and cost.[25,26]

Graphene has attracted wide attention in both industry and academia owing to its excellent thermal, electrical and mechanical properties, etc.[27−30] Herein, one of the most remarkable properties of graphene is its extremely ultra-high thermal conductivity and, in theory, the in-plane thermal conductivity is reported to be higher than 5000 W/(m K),[31] well above other known thermally conductive fillers. Therefore, graphene is considered to be the most promising fillers to improve the thermal conductivities of the polymer composites. For example, Fang et al.[32,33] successfully fabricated graphene foam/polydimethylsiloxane composites, and the improved in-plane λ value was 28.77 W/(m K) at 11.62 wt % graphene foam. Song et al.[31] reported a high in-plane λ value of 2.03 W/(m K) in the graphene/silicone rubber multilayered films at 2.53 wt % graphene loading. However, graphene always tends to aggregate easily due to its strong intermolecular $\pi−\pi$ interaction, resulting in poor dispersion in the polymer matrix.[34]

Many physical and chemical methods (such as functionalization, ball milling, sonication, etc.) have been employed to prevent the aggregation of graphene.[35−37] However, these techniques always result in inevitable structural damages and mechanical property loss of graphene.[38] Samulski et al.[39] proved that the aggregation of graphene could be effectively restricted by introducing metal nanoparticles on the surface of graphene. Metal nanoparticles, acting as "spacers", maintained the single layer structure of graphene, finally ensured its intrinsically excellent properties. Meanwhile, it can also endow graphene other unique properties exhibited by metal nanoparticles. Several metal nanoparticles, such as platinum (Pt),[40] nickel (Ni),[41] ferrum (Fe),[42] silver (Ag), etc. had been successfully decorated on the graphene surface. Among them, Ag has received widespread attention due to its highest thermal and

electrical conductivity. Besides, the preparation process of Ag nanoparticles is relatively easy. However, there is no related report about the thermal conductivity of the Ag/graphene composite fillers, let alone the thermally conductive polymer composites filled with Ag/graphene composite fillers.

In this work, highly thermally conductive silver/reduced graphene oxide/polyimide ((Ag/rGO)/PI) nanocomposites were successfully designed and prepared using electrospinning the in situ polymerized Ag/rGO/polyamide suspension followed by a hot-press technique. Ag/rGO fillers with a "point-plane" structure were first prepared using a "one-pot" reaction by synchronous reduction of Ag+ and GO solution via glucose. Ag nanoparticles acted as "spacers" to maintain the high specific surface area and increase the cross-plane thermal conductivity of rGO fillers. The ultraviolet-visible spectrum (UV−vis), thermal gravimetric analyses (TGA), X-ray photoelectron spectroscopy (XPS), X-ray diffraction (XRD), and transmission electron microscopy (TEM) were performed to analyze and characterize the structures and properties of the Ag/rGO fillers. In addition, the mass ratio of rGO to Ag and the total Ag/rGO fillers mass fraction affecting the λ values, thermal stabilities, and mechanical properties of the (Ag/rGO)/PI nanocomposites were also studied in detail. Moreover, an improved thermal conduction model on the basis of the effective medium theory (EMT) and Fourier law was also established to calculate the theoretical λ values of the (Ag/rGO)/PI nanocomposites.

2. MATERIALS PREPARATION

2.1. Materials. 4,4′-Oxydiphthalic anhydride (ODPA, AR, 99%) was purchased from Sun Chemical Technology Co., Ltd., China. 4-[3-(4-Aminophenoxy)phenoxy]aniline (APB, AR, 99%) was received from Changzhou Sunlight Medicine Raw Material Co., Ltd., China. A natural graphite flake (99.8%) was obtained from Alfa Aesar (China) Chemistry Co., Ltd. with an average diameter of 325 mesh. Glucose (D-glucose, AR, 198.17 g/mol) and AgNO3 (AR, 169.87 g/mol) were both purchased from Guangdong Guanghua Sci-Tech Co., Ltd., China. Tetrahydrofuran (THF, 99%) and N,N-dimethylacetamide (DMAc, 99%) were provided by Tianjin Tianli Chemical Co., Ltd. China.

2.2. Fabrication of the (Ag/rGO)/PI Nanocomposites. *2.2.1. Preparation of Ag/rGO Fillers.* GO was first obtained from a natural graphite flake based on a modified Hummers method.[36] For a typical procedure for decorating Ag nanoparticles on the surface of rGO, 0.0945 g of AgNO3 was added into 10.5 mL of deionized water to form silver ammonia solution, followed by mixing with 60 mL of homogeneous GO aqueous dispersion (1 mg/mL). Then, 0.16 g of D-glucose and 1 mL of EtOH were gradually added into the above

mixture, and the mixture was treated at 140 °C for 6 h in the Teflon-lined reaction vessel and cooled down to ambient temperature. Finally, the mixture was filtered, washed, and dried for 24 h. Ag/rGO fillers with different mass ratios of rGO to Ag nanoparticles (rGO:Ag = 1, 2, 3, 4, 5, wt:wt) were fabricated by changing the mass fractions of AgNO₃. Figure 1 shows the schematic diagram of the preparation of the Ag/rGO fillers.

2.2.2. Fabrication of the (Ag/rGO)/PI Nanocomposites. The (Ag/rGO)/PI nanocomposites were prepared in accordance with previous work.[36] Briefly, a quantity of Ag/rGO fillers was dispersed uniformly under ultrasonic treatment for 30 min in 20 mL of a mixed solvent of DMAc/THF (DMAc:THF = 3:2, wt:wt). The mixture was then transferred to an anhydrous three-necked flask with a mechanical stirrer and nitrogen atmosphere in an ice-bath. Then, 5 mmol of APB and 5 mmol of ODPA were sequentially added into the above flask and stirred for 3 h at 5 °C, to obtain a homogeneous (Ag/rGO)/polyamide electrospun solution. After this, the (Ag/rGO)/polyamide electrospun fibers were prepared via electrospinning technology with a voltage of 20 kV, receiving distance of 30 cm, and a rotation speed of 40 m/min, followed by removing the residual solvent at 80 °C for 4 h, and then treated with a thermal imidization procedure of 120 °C/1 h + 200 °C/1 h + 250 °C/1 h, to obtain the corresponding (Ag/rGO)/PI electrospun fibers. Finally, the (Ag/rGO)/PI electrospun fibers were placed by hand and then compacted at 320 °C and 10 MPa for another 40 min to obtain (Ag/rGO)/PI nanocomposites.

2.3. Characterization. Ultraviolet-visible (UV−vis) spectrophotometer (BlueStar, LabTech) was used to characterize the absorption spectrum of the samples over the wavelength of 200−900 nm, and the test concentration was 0.05 mg/mL. X-ray photoelectron spectroscopy (XPS, Kratos Axis Ultra DLD, UK) was performed to measure the relative element content on the surface of the samples. X-ray diffraction (XRD) patterns of the samples were tested using an XRD-7000 (Shimadzu, Japan) with Cu Kα radiation. Transmission electron microscopy (TEM, Talos F200X, FEI) was performed to investigate the level of exfoliation and dispersion of the samples. A scanning electron microscope (SEM, VEGA3-LMH, TESCAN Corp., Czech Republic) was employed to observe the surface morphologies of the samples. A thermal constant analyzer instrument (Hot Disk TPS2200, AB Corp., Sweden) was used to measure the thermal conductivities of the samples (20 mm × 20 mm × 2 mm) according to the standard of ISO 22007-2: 2008. A Fluke infrared thermal imager (Ti 450, Fluke) was used for the thermal measurement on a plate at a constant temperature of 90 °C. The dimension of all samples was 20 mm × 20 mm × 2 mm and the distance between the sample and the infrared thermal imager was about 10 cm. The glass transition temperature (T_g) of the samples was measured on a DSC1 (Mettler-Toledo Corp., Switzerland) with a heating rate of 10 °C/min under a nitrogen atmosphere (flow rate of 50 mL/min). The decomposition temperatures of the samples were measured by thermal gravimetric analyses (TGA, STA 449F3, NETZSCH Corp., Germany) from 40 to 900 °C at a heating rate of 10 °C/min under an argon atmosphere (flow rate of 20 mL/min). Nanoindentation tests were performed using a Nanoindenter (TI-980, Hysitron) equipped with a Berkovich diamond tip to test the reduced modulus and Brinell hardness of the samples. The maximum loading force was 9 mN, the loading rate was 1.8 mN/s, and the holding time was 2 s.

3. RESULTS AND DISCUSSION

3.1. Characterization of GO and Ag/rGO. Figure 1 shows the schematic diagram of the preparation for the Ag/rGO fillers. The oxygen groups on the surface of GO contribute to the negatively charged surface, to provide initial active nucleation sites and attach Ag⁺ due to electrostatic interaction. On one hand, the hydroxyl groups on the surface of GO provide phenolic protons, which can be further deprotonated to form phenate anions. Such anions can contribute one electron to Ag⁺, reducing it to Ag nanoparticles. On the other hand, Ag⁺ can promote glucose oxidized to glucuronic acid in the presence of ammonia and oxygen. Then, the introduction of glucuronic acid

results in the reduction of GO and can be further converted into glucuronolactone. The addition of glucose can also promote the Ag precursor being reduced to Ag, finally enable the growth of Ag nanoparticles.[43]

The observed maximum absorption peak near 233 nm and an unobvious absorption peak around 293 nm in GO, Figure 2a,
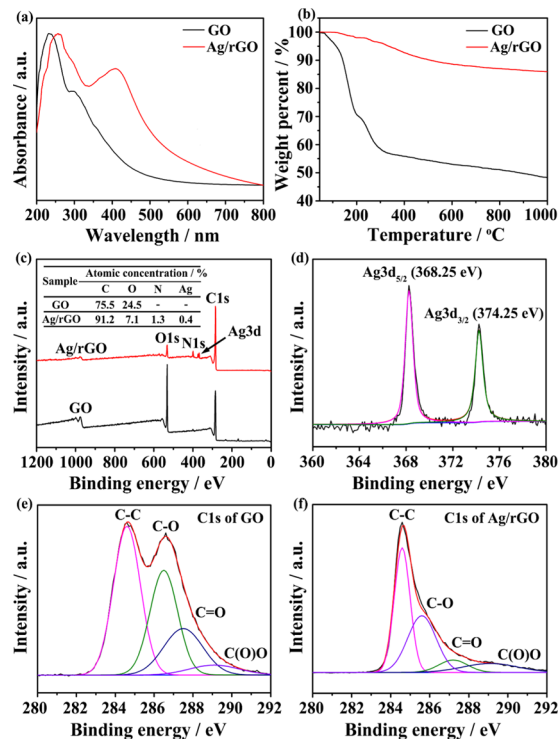

Figure 2. UV−vis, TGA, and XPS curves of GO and Ag/rGO fillers. (a) UV−vis spectrum, (b) TGA, (c) the XPS full spectrum, and (d, e, f) the XPS narrow spectrum.

correspond to the π−π* electron transition (C=C) and n−π* electron transition (C=O), respectively.[44] For Ag/rGO, the absorption peak at 233 nm presents a red shift to 258 nm. The appeared new absorption peak at about 410 nm is mainly ascribed to the absorption peak of Ag nanoparticles and its surface plasmon resonance absorption.[44] The red shift suggests that GO has been reduced and the electronic conjugation structure of graphene has been restored successfully.[45]

The main weight loss of GO from 100 to 300 °C, Figure 2b, is mainly attributed to the decomposition of unstable oxygen groups. In addition, the low weight loss from 400 to 1000 °C is attributed to the decomposition of more stable oxygen groups.[46] For Ag/rGO, the total weight loss is much less than that of GO, and there is only 4% weight loss at 300 °C. No significant weight loss was observed from 400 to 1000 °C. The reason is that the removal of unstable oxygen groups is in favor of increasing the thermal stability of Ag/rGO. Moreover, there are lots of hydroxyl groups and carboxyl groups on the glucose oxidization products, which can form hydrogen bonds with the oxygen groups on the surface of rGO, to improve the thermal stability of rGO.[45] Besides, Ag nanoparticles on the rGO sheets can also increase the final residues.

To investigate the mechanism of the Ag nanoparticles decorating on the rGO, the interaction between the Ag and rGO is studied using XPS, as shown in Figure 2c−f. Figure 2c depicts the XPS full spectrum of GO and Ag/rGO. GO only

shows two peaks of C 1s and O 1s, and a new peak of Ag 3d appears for Ag/rGO. Besides, Ag/rGO shows an obvious increase in the C/O atomic ratio (13/1) in comparison to that of GO (3/1), indicating a successful reduction of GO. The observed two key peaks at 368.25 and 374.25 eV in Figure 2d correspond to the metallic Ag^0 $3d_{5/2}$ and Ag^0 $3d_{3/2}$,[47] indicating the valence state of Ag^0. It reveals that the Ag^+ ions have been reduced by glucose. Figure 2e,f presents the C 1s XPS spectra of GO and Ag/rGO, respectively. The four peaks correspond to C-C (~284.6 eV), C-O (~286.0 eV), C═O (~287.5 eV), and C(O)O (~289.0 eV).[48] The corresponding peak intensities of oxygen bonding (C-O, C═O, C(O)O) in Ag/rGO are much lower than those of GO, revealing the removal of oxygen groups. The above analyses indicate that GO has been successfully reduced by glucose, and only metallic Ag nanoparticles are successfully decorated on the rGO.

Figure 3a presents the XRD patterns of GO and Ag/rGO. GO has a feature diffraction peak at ~11° (001) with a *d*-spacing of
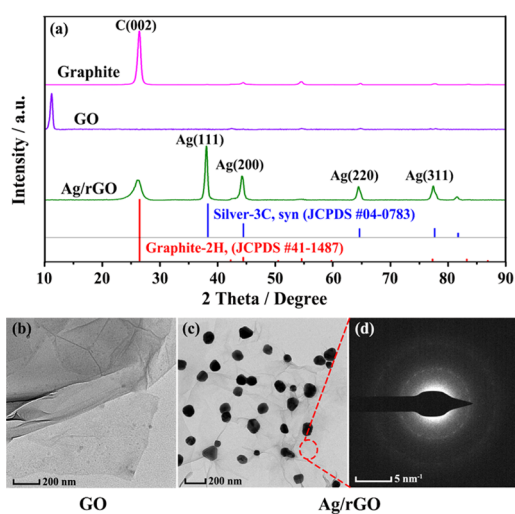

Figure 3. XRD patterns and TEM images of GO and Ag/rGO fillers. (a) XRD, (b) TEM of GO, (c) TEM of Ag/rGO, and (d) SAED of Ag/rGO.

0.79 nm, which is ascribed to the introduction of oxygen groups on carbon nanosheets. For Ag/rGO, a diffraction peak at ~26° (002) with a *d*-spacing of 0.34 nm appears,[49] consistent with pristine graphene. It indicates that GO has been reduced successfully and the obtained Ag/rGO possesses a perfect crystal structure. In addition, XRD patterns of Ag/rGO also display typical diffraction peaks at 38, 44, 64, and 77°, corresponding to Ag (111), (200), (220), and (311) crystal face, respectively. No observed Ag^+ diffraction pattern in the XRD pattern of Ag/rGO reveals only Ag on the surface of Ag/rGO fillers.

TEM images in Figure 3b show that the GO exhibits a corrugated surface and flat edges, and also presents large flakes with a few layers. Herein, the corrugation of GO is mainly ascribed to the disruption of sp^2 carbon by the introduction of sp^3 hybridized carbon during the oxidation procedure.[50] Figure 3c presents the TEM image of Ag/rGO. rGO presents a homogeneous and flat surface, whereas the corresponding edges tend to scroll, to form ribbons with corrugation in some folded regions. Ag nanoparticles with an average diameter of 90 nm are well distributed on the rGO. The corresponding Ag/rGO fillers present a strong diffraction ring (Figure 3d), indicating the multiple crystals of Ag/rGO fillers.[47]

3.2. Characterization of Pure PI and (Ag/rGO)/PI Electrospun Fibers.

Morphologies of pure PI and (Ag/rGO)/PI electrospun fibers are observed by SEM, shown in Figure 4. All of the electrospun fibers are directionally arranged
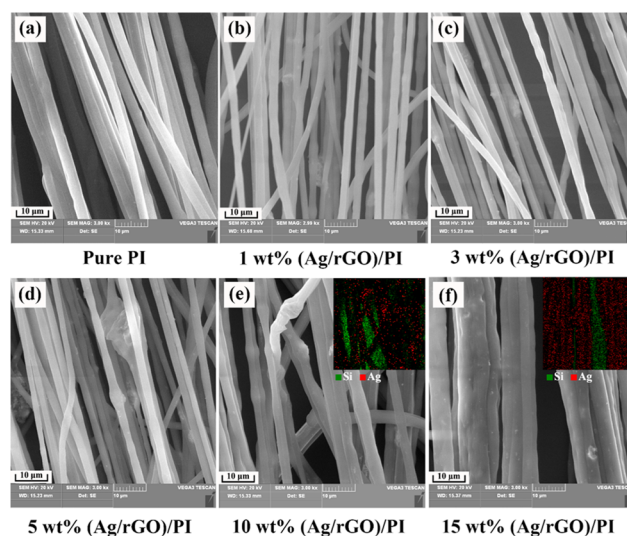

Figure 4. SEM images of pure PI and (Ag/rGO)/PI electrospun fibers. Insets in (e) and (f) are EDS testing.

and present a relatively uniform diameter. With increasing the mass fraction of Ag/rGO fillers, the average diameter of the (Ag/rGO)/PI electrospun fibers is decreased first and then increased, but the direction disorder of the obtained (Ag/rGO)/PI electrospun fibers becomes more apparent. The main reason is that the introduction of Ag/rGO fillers increases the electrical conductivity of the (Ag/rGO)/polyamide electrospun solution, which is good for increasing the charge density and axial whip instability of the jet, finally to decrease the diameter of (Ag/rGO)/PI electrospun fibers.[51] With further increasing the Ag/rGO filler loading, the electrical conductivity of the (Ag/rGO)/polyamide electrospun solution is greatly increased, and the flow rate of the jet is also increased, which increase the diameter of (Ag/rGO)/PI electrospun fibers and a more disordered fibers' arrangement. Meanwhile, the solution viscosity is also increased with increasing the Ag/rGO filler loading, resulting in an increased diameter of the (Ag/rGO)/PI electrospun fibers.[52] In addition, with increasing the Ag/rGO filler loading, the beads also appear on the (Ag/rGO)/PI electrospun fibers. The main reason is that the axially symmetric tensor instability of the jet increases with increasing the conductivity of the (Ag/rGO)/PI electrospun solution, changing the radial direction and leading to the formation of beads. Besides, the embedded Ag/rGO fillers in or on the (Ag/rGO)/PI electrospun fibers can also result in the formation of beads. In addition, the EDS analyses also demonstrate the presence of Ag nanoparticles on the (Ag/rGO)/PI electrospun fibers (insert in Figure 4e,f).

3.3. Properties of the (Ag/rGO)/PI Nanocomposites.

The mass ratio of rGO to Ag affecting the λ values of the (Ag/rGO)/PI nanocomposites is presented in Figure 5. For a given loading of Ag/rGO fillers (5 and 10 wt %), when the mass ratio of rGO to Ag is 4:1, the corresponding λ value of the (Ag/rGO)/PI nanocomposites reaches the maximum of 0.90 W/(m K) (5 wt %) and 1.54 W/(m K) (10 wt %), respectively. As shown in Figure 6, with decreasing the mass fraction of Ag, the stack and agglomeration of the rGO are significantly reduced, beneficial to
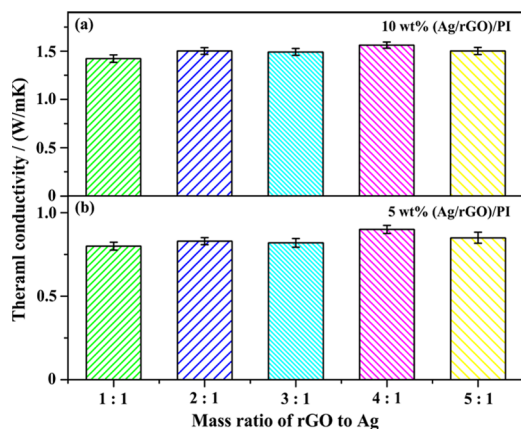
Figure 5. Mass ratio of rGO to Ag influencing on the λ values of the (Ag/rGO)/PI nanocomposites.
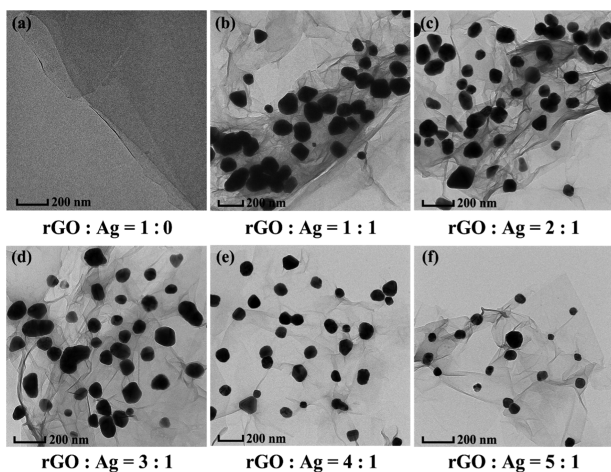

Figure 6. TEM images of Ag/rGO fillers with different mass ratio of rGO to Ag. (a) 1:0, (b) 1:1, (c) 2:1 (d) 3:1 (e) 4:1 (f) 5:1.

improving the thermal conductivities. In addition, the corresponding average diameter of the Ag nanoparticles is also reduced, and the distribution of the Ag nanoparticles on the rGO is more uniform. Ag nanoparticles serve as "spacers" between rGO, to maintain rGO with high specific surface area and increase the thermal conductivities across the rGO plane.[53]

Figure 7a shows the mass fraction of Ag/rGO and rGO fillers influencing the λ values of the (Ag/rGO)/PI (mass ratio of rGO

to Ag is 4:1) and rGO/PI nanocomposites. Continuous increase in the λ values of the rGO/PI and (Ag/rGO)/PI nanocomposites can be observed with increasing the mass fraction of rGO and Ag/rGO fillers. The λ of the (Ag/rGO)/PI nanocomposites with 15 wt % Ag/rGO fillers reaches the maximum value of 2.12 W/(m K), about 8 times as high as that of pure PI (0.27 W/(m K)), also higher than that of rGO/PI nanocomposites (1.51 W/(m K)). Besides, the (Ag/rGO)/PI nanocomposites also have a higher λ value than that of the previously reported λ value by introducing single Ag nanoparticles into the polymer.[54] Interestingly, the corresponding λ values of the (Ag/rGO)/PI nanocomposites are improved sharply when the mass fraction of Ag/rGO fillers exceeds 3 wt %. It can be attributed to the formed thermally conductive paths arising from sufficient Ag/rGO fillers in the (Ag/rGO)/PI nanocomposites. Moreover, Ag nanoparticles also bridge the gaps between the rGO and PI matrix and further benefit phonon transportation, resulting in an obvious enhancement in λ values.

In addition, the aggregation of rGO can be effectively restricted by introducing Ag nanoparticles. Besides, SEM images of the fracture surfaces for the (Ag/rGO)/PI nanocomposites (inserts in Figure 7a) also show that the Ag/rGO fillers are well aligned and parallel to a specific direction. This benefits the formation of an end-to-end structure of Ag/rGO networks and thus gives relatively higher thermal conductivities.[55] Figure 7b presents the infrared thermograms of the (Ag/rGO)/PI nanocomposites. The corresponding surface temperature increases more rapidly with a relatively higher Ag/rGO loading, indicating a higher heat dissipation ability. Such results correspond well to the experimental results as shown in Figure 7a. Besides, the surface temperature distribution is relatively uniform, indicating a macroscopic uniform distribution of the Ag/rGO fillers.

Table 1 shows the reported λ values of the polymer composites with diverse fillers.[56−60] The (Ag/rGO)/PI nanocomposites show relatively higher λ values and thermal conductivity enhancement (defined as $(\lambda_{composite} - \lambda_{matrix})/\lambda_{matrix}$) with a relatively lower mass fraction of fillers. The primary reasons are summarized as follows. (1) Ag/rGO fillers possess high λ value, Ag nanoparticles act as "spacers", to maintain rGO with a high specific surface area as well as ultrahigh thermal conductivity. (2) Ag nanoparticles bridge the rGO gaps in the cross-plane direction, in favor of decreasing the contact thermal resistance and increasing the cross-plane thermal conductivity. (3) Ag/rGO fillers are well aligned with the PI electrospun fibers, beneficial for forming an end-to-end
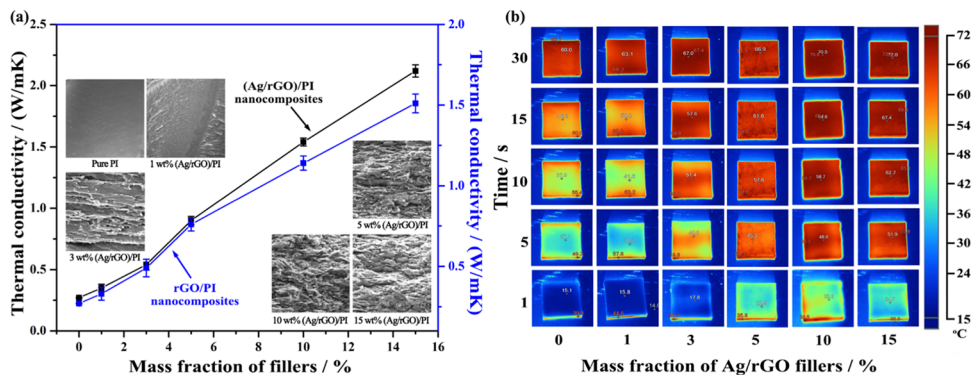

Figure 7. Thermal conductivities of the (Ag/rGO)/PI nanocomposites. (a) Mass fraction of Ag/rGO and rGO influencing on the λ values of the (Ag/rGO)/PI and rGO/PI nanocomposites, respectively, (b) Infrared thermal images of (Ag/rGO)/PI nanocomposites.

Table 1. Comparison in λ Values for Different Thermally Conductive Polymer Composites

filler composition and loading	polymer matrix	λ (W/(m K))	enhancement (%)	reference
15 wt % Ag/rGO	polyimide (PI)	2.12	685	our work
60 wt % Cu@rGO	epoxy	1.40	450	ref 56
20 wt % SiO$_2$@RGO	epoxy	0.29	26	ref 57
20 wt % BN@GO	epoxy	0.78	255	ref 58
20 wt % TrGO	low density polyethylene (LDPE)	0.84	333	ref 59
20 wt % GNPs	polycarbonate (PC)	1.76	350	ref 60

structure of Ag/rGO networks and finally resulting in relatively higher thermal conductivities.[61]

To deeply understand the synergistic effect of Ag/rGO fillers on enhancing the λ values of (Ag/rGO)/PI nanocomposites, an improved thermal conduction model is established on the basis of modified EMT and Flourier law in this work (detailed information is shown in the Supporting Information). The λ values obtained by our improved thermally conductive model and equation (eq 1, from eq S10) and several classical models, such as Maxwell, Russell, and Bruggeman model, are plotted in Figure 8. It can be observed that the theoretical λ values
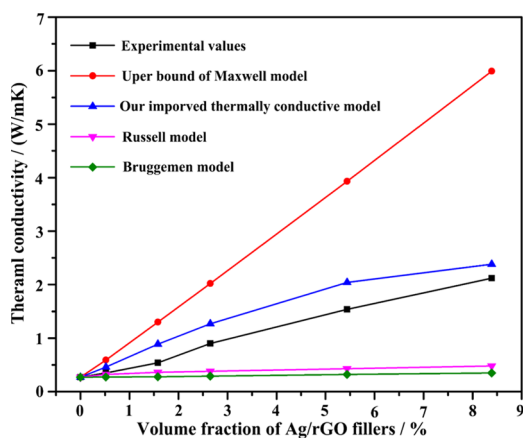

Figure 8. Experimental λ values of the (Ag/rGO)/PI nanocomposites and theory λ values from our established and proposed improved thermal conduction model, and classical Maxwell, Russell, and Bruggeman models.

calculated by our improved thermal conduction model are relatively closer to the experimental results compared with those of the above traditional models, more suitable for the (Ag/rGO)/PI nanocomposites.

$$\lambda' \approx \left\{ \frac{3\lambda_{\parallel}^{*}\lambda_{\parallel}^{*}\int_0^{2\lambda_{\perp}^{*}}\sqrt{\lambda_{\perp}^{*}}\left[(T_w - T_i)\left(\frac{\sqrt{12\alpha\tau}-z}{\sqrt{12\alpha\tau}}\right)^2 - t_i\right]\left[\frac{2z\lambda_{\perp}^{*}-z^2}{\lambda_{\perp}^{*2}}\right]dz}{4(T_w - 2T_i)} \right\}^{2/7}$$

(1)

The DSC and TGA curves of pure PI and (Ag/rGO)/PI nanocomposites (mass ratio of rGO to Ag is 4:1) are shown in Figure 9 and the relevant data is shown in Table S1. The T_g value of the (Ag/rGO)/PI nanocomposites increases with increasing the Ag/rGO filler loading. The (Ag/rGO)/PI nanocomposites with 15 wt % Ag/rGO have a maximum T_g value of 216.1 °C, about 11 °C higher than pure PI (205.2 °C). Besides, the corresponding glass transition zone becomes increasingly inconspicuous. The main reason is that PAA molecular chains present orientation and alignment during the electrospinning process, and the free volume of PAA molecules becomes smaller. On the other hand, Ag/rGO might occupy some free volume and limit the thermal motion of PAA molecular chains.[62] With increasing the Ag/rGO filler loading, the specific heat capacity of the (Ag/rGO)/PI nanocomposites presents little change, and the baseline from the DSC curve toward the endothermic direction gets smaller and smaller accordingly.[63]

As seen from Table S1, in comparison to that of the pure PI matrix, the thermal decomposition temperature (T_5 and T_{30}) and the $T_{Heat\ resistance\ index}$ (T_{HRI}) value[64] of the (Ag/rGO)/PI nanocomposites are greatly enhanced with increasing the Ag/rGO filler loading. The corresponding T_{HRI} value of the (Ag/rGO)/PI nanocomposites with 15 wt % Ag/rGO is enhanced from 272.7 °C for the pure PI matrix to 298.6 °C. Besides, the enhancement of the T_5 value for (Ag/rGO)/PI nanocomposites with 15 wt % Ag/rGO is 21 °C, higher than previous reports about graphene/PI composites.[65] The electrospinning process can realize the Ag/rGO fillers coated on or embedded in the PI electrospun fibers, in favor of forming a carbon layer network at
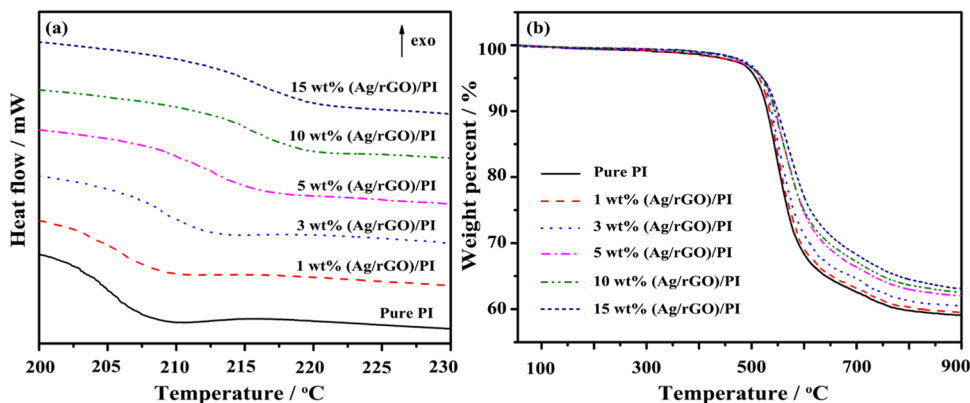

Figure 9. DSC and TGA curves of the pure PI matrix and (Ag/rGO)/PI nanocomposites. (a) DSC and (b) TGA.
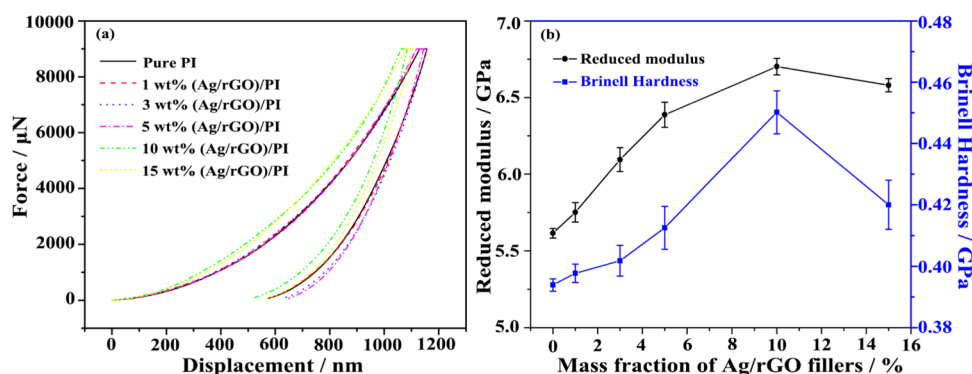
Figure 10. Nanoindentation tests for the pure PI matrix and (Ag/rGO)/PI nanocomposites. (a) Load-penetration depth curves. (b) Nanoindentation reduced modulus and Brinell hardness.

higher temperatures, finally inhibiting the effuse of decomposition products.[66]

Figure 10 shows the nanoindentation results of pure PI and (Ag/rGO)/PI nanocomposites (mass ratio of rGO to Ag is 4:1). With increasing the Ag/rGO filler loading, the reduction modulus (E_r) and Brinell hardness (HB) of the (Ag/rGO)/PI nanocomposites are increased first and then decreased. When the mass fraction of Ag/rGO fillers is 10 wt %, the relevant E_r and HB reach the maximum of 6.70 and 0.45 GPa, increased by 19.2 and 15.4%, compared with pure PI (E_r = 5.62 GPa, HB = 0.39 GPa), respectively. The primary reason is that, with increasing the Ag/rGO filler loading, the increasing carbon content of the (Ag/rGO)/PI nanocomposites is in favor of increasing the modulus and hardness for the (Ag/rGO)/PI nanocomposites. In addition, Ag/rGO fillers possess excellent mechanical properties and can bear the load and pin dislocation movement of PI molecular chains during the deformation. However, the layered structure of Ag/rGO fillers results in weak bonding forces between rGO. With further increasing the Ag/rGO filler loading, Ag/rGO fillers are much easier to stack and be piled up, and probably form inner defects in the (Ag/rGO)/PI nanocomposites, resulting in the decreases of E_r and HB values.[67]

4. CONCLUSIONS

Unique Ag/rGO fillers with the "point-plane" structure were successfully fabricated by employing a "one-pot" method by synchronous reduction of Ag^+ and GO solution via glucose. UV−vis, TGA, XPS, XRD, and TEM analyses indicated that Ag/rGO fillers belonged to multiple crystals and Ag nanoparticles with an average diameter of 90 nm were distributed on the surface of rGO uniformly. The electrospinning process helped the Ag/rGO fillers to align along the PI electrospun fibers, and the Ag/rGO fillers were embedded in or on the PI electrospun fibers. The λ, T_g and T_{HRI} values of the (Ag/rGO)/PI nanocomposites were all increased with increasing the Ag/rGO filler loading. When the mass ratio of rGO to Ag was 4:1, and the total mass fraction of Ag/rGO fillers was 15 wt %, the relevant λ value of the (Ag/rGO)/PI nanocomposites reached the maximum of 2.12 W/(m K), about 8 times as high as pure PI (λ of 0.27 W/(m K)). Furthermore, the theoretical λ values calculated by our improved thermal conduction model were relatively closer to the experimental λ values compared with those calculated from other classical models, more suitable for the (Ag/rGO)/PI nanocomposites. In addition, the corresponding T_g and T_{HRI} values of the (Ag/rGO)/PI nanocomposites were also enhanced to 216.1 and 298.6 °C, respectively.

■ ASSOCIATED CONTENT

ⓈSupporting Information

The Supporting Information is available free of charge on the ACS Publications website at DOI: 10.1021/acsami.9b10161.

> Experimental section; theoretical derivations of the thermal conductivity; schematic diagram of established and proposed improved thermal conduction model (Figure S1); characteristic thermal data of the pure PI matrix and the (Ag/rGO)/PI nanocomposites (Tables S1) (PDF)

■ AUTHOR INFORMATION

Corresponding Authors
*E-mail: gjw@nwpu.edu.cn, nwpugjw@163.com (J. Gu).
*E-mail: nanomaterials2000@gmail.com, zguo10@utk.edu (Z. Guo).

ORCID ⓘ
Jie Kong: 0000-0002-9405-3204
Zhanhu Guo: 0000-0003-0134-0210

Author Contributions
All authors have reviewed and given approval to the final version of the manuscript.

Notes
The authors declare no competing financial interest.

■ REFERENCES

(1) Li, S.; Zheng, Q.; Lv, Y.; Liu, X.; Wang, X.; Huang, P. Y.; Cahill, D. G.; Lv, B. High Thermal Conductivity in Cubic Boron Arsenide Crystals. *Science* **2018**, *361*, 579−581.

(2) Zhang, D. L.; Zha, J. W.; Li, C. Q.; Li, W. K.; Wang, S. J.; Wen, Y.; Dang, Z. M. High Thermal Conductivity and Excellent Electrical

Insulation Performance in Double-Percolated Three-Phase Polymer Nanocomposites. *Compos. Sci. Technol.* **2017**, *144*, 36−42.

(3) Zhang, L.; Deng, H.; Fu, Q. Recent Progress on Thermal Conductive and Electrical Insulating Polymer Composites. *Compos. Commun.* **2018**, *8*, 74−82.

(4) Wang, Z. G.; Gong, F.; Yu, W. C.; Huang, Y. F.; Zhu, L.; Lei, J.; Xu, J. Z.; Li, Z. M. Synergetic Enhancement of Thermal Conductivity by Constructing Hybrid Conductive Network in the Segregated Polymer Composites. *Compos. Sci. Technol.* **2018**, *162*, 7−13.

(5) Liang, C. B.; Qiu, H.; Han, Y. Y.; Gu, H. B.; Song, P.; Wang, L.; Kong, J.; Cao, D. P.; Gu, J. W. Superior Electromagnetic Interference Shielding 3D Graphene Nanoplatelets/Reduced Graphene Oxide Foam/Epoxy Nanocomposites with High Thermal Conductivity. *J. Mater. Chem. C* **2019**, *7*, 2725−2733.

(6) Zhang, Y.; Ren, B.; Xie, S.; Cai, Y.; Wang, T.; Feng, Z.; Tang, J.; Chen, Q.; Xu, J.; Xu, L.; Zheng, J. Multiple Physical Cross-Linker Strategy to Achieve Mechanically Tough and Reversible Properties of Double-Network Hydrogels in Bulk and on Surfaces. *ACS Appl. Polym. Mater.* **2019**, *1*, 701−713.

(7) Song, N.; Cao, D. L.; Luo, X.; Guo, Y. Q.; Gu, J. W.; Ding, P. Aligned Cellulose/Nanodiamond Plastics with High Thermal Conductivity. *J. Mater. Chem. C* **2018**, *6*, 13108−13113.

(8) Kashfipour, M.; Mehra, N.; Zhu, J. A Review on the Role of Interface in Mechanical, Thermal and Electrical Properties of Polymer Composites. *Adv. Compos. Hybrid Mater.* **2018**, *1*, 415−439.

(9) Yu, W.; Liu, C. Q.; Qiu, L.; Zhang, P.; Ma, W. G.; Yue, Y. N.; Xie, H. Q.; Larkin, L. S. Advanced Thermal Interface Materials for Thermal Management. *Eng. Sci.* **2018**, *2*, 1−3.

(10) Li, H.; Tie, J.; Li, J. Z.; Ye, M.; Zhang, H.; Zhang, X. Y.; Pan, Y. Y.; Wang, Y. Y.; Quhe, R. G.; Pan, F.; Lu, J. High-Performance sub-10-nm Monolayer Black Phosphorene Tunneling Transistors. *Nano Res.* **2018**, *11*, 2658−2668.

(11) Mehra, N.; Mu, L. W.; Zhu, J. H. Developing Heat Conduction Pathways Through Short Polymer Chains in a Hydrogen Bonded Polymer System. *Compos. Sci. Technol.* **2017**, *148*, 97−105.

(12) Liang, T.; Qi, L.; Ma, Z.; Xiao, Z.; Wang, Y.; Liu, H.; Zhang, J.; Guo, Z.; Liu, C.; Xie, W.; Ding, T.; Lu, N. Experimental Study on Thermal Expansion Coefficient of Composite Multi-Layered Flaky Gun Propellants. *Composites, Part B* **2019**, *166*, 428−435.

(13) Ji, T. X.; Feng, Y. Y.; Qin, M. M.; Li, S. W.; Zhang, F.; Lv, F.; Feng, W. Thermal Conductive and Flexible Silastic Composite Based on a Hierarchical Framework of Aligned Carbon Fibers-Carbon Nanotubes. *Carbon* **2018**, *131*, 149−159.

(14) Pan, C.; Kou, K. C.; Jia, Q.; Zhang, Y.; Wu, G. L.; Ji, T. Z. Improved Thermal Conductivity and Dielectric Properties of hBN/PTFE Composites via Surface Treatment by Silane Coupling Agent. *Composites, Part B* **2017**, *111*, 83−90.

(15) Feng, C. P.; Bai, L.; Shao, Y.; Bao, R. Y.; Liu, Z. Y.; Yang, M. B.; Chen, J.; Ni, H. Y.; Yang, W. A Facile Route to Fabricate Highly Anisotropic Thermally Conductive Elastomeric POE/NG Composites for Thermal Management. *Adv. Mater. Interfaces* **2018**, *5*, No. 1700946.

(16) Jiang, F.; Cui, S. Q.; Song, N.; Shi, L. Y.; Ding, P. Hydrogen Bond-Regulated Boron Nitride Network Structures for Improved Thermal Conductive Property of Polyamide-Imide Composites. *ACS Appl. Mater. Interfaces* **2018**, *10*, 16812−16821.

(17) Pan, C.; Kou, K. C.; Zhang, Y.; Li, Z. Y.; Wu, G. L. Enhanced Through-Plane Thermal Conductivity of PTFE Composites with Hybrid Fillers of Hexagonal Boron Nitride Platelets and Aluminum Nitride Particles. *Composites, Part B* **2018**, *153*, 1−8.

(18) Guo, Y.; Lyu, Z.; Yang, X.; Lu, Y.; Ruan, K.; Wu, Y.; Kong, J.; Gu, J. Enhanced Thermal Conductivities and Decreased Thermal Resistances of Functionalized Boron Nitride/Polyimide Composites. *Composites, Part B* **2019**, *164*, 732−739.

(19) Zhou, Y.; Wu, S.; Liu, F. High-Performance Polyimide Nanocomposites with Polydopamine-Coated Copper Nanoparticles and Nanowires for Electronic Applications. *Mater. Lett.* **2019**, *237*, 19−21.

(20) Jiang, Y. L.; Li, M. Y.; Chen, C.; Xue, Z. G.; Xie, X. L.; Zhou, X. P.; Mai, Y. W. Effect of Elastic Modulus Mismatch of Epoxy/Titanium

Dioxide Coated Silver Nanowire Composites on the Performance of Thermal Conductivity. *Compos. Sci. Technol.* **2018**, *165*, 206−213.

(21) Olifirov, L. K.; Kaloshkin, S. D.; Zhang, D. Study of Thermal Conductivity and Stress-Strain Compression Behavior of Epoxy Composites Highly Filled with Al and Al/*f*-MWCNT Obtained by High-Energy Ball Milling. *Composites, Part A* **2017**, *101*, 344−352.

(22) Zhou, W.; Gong, Y.; Tu, L.; Xu, L.; Zhao, W.; Cai, J.; Zhang, Y.; Zhou, A. Dielectric Properties and Thermal Conductivity of Core-Shell Structured Ni@NiO/Poly (vinylidene fluoride) Composites. *J. Alloys Compd.* **2017**, *693*, 1−8.

(23) Qu, Z.; Shi, M.; Wu, H.; Liu, Y.; Jiang, J.; Yan, C. An Efficient Binder-Free Electrode with Multiple Carbonized Channels Wrapped by NiCo$_2$O$_4$ Nanosheets for High-Performance Capacitive Energy Storage. *J. Power Sources* **2019**, *410−411*, 179−187.

(24) Shen, X.; Wang, Z. Y.; Wu, Y.; Liu, X.; He, Y. B.; Zheng, Q. B.; Yang, Q. H.; Kang, F. Y.; Kim, J. K. A Three-Dimensional Multilayer Graphene Web for Polymer Nanocomposites with Exceptional Transport Properties and Fracture Resistance. *Mater. Horiz.* **2018**, *5*, 275−284.

(25) Mehra, N.; Mu, L. W.; Ji, T.; Yang, X. T.; Kong, J.; Gu, J. W.; Zhu, J. H. Thermal Transport in Polymeric Materials and Across Composite Interfaces. *Appl. Mater. Today* **2018**, *12*, 92−130.

(26) Yang, X. T.; Liang, C. B.; Ma, T. B.; Guo, Y. Q.; Kong, J.; Gu, J. W.; Chen, M. J.; Zhu, J. H. A Review on Thermally Conductive Polymeric Composites: Classification, Measurement, Model & Equations, Mechanism and Fabrication Methods. *Adv. Compos. Hybrid Mater.* **2018**, *1*, 207−230.

(27) Sun, H. Y.; Li, X. M.; Li, Y. C.; Chen, G. X.; Liu, Z. D.; Alam, F. E.; Dai, D.; Li, L.; Tao, L.; Xu, J. B.; Fang, Y.; Li, X. S.; Zhao, P.; Jiang, N.; Chen, D.; Lin, C. T. High-Quality Monolithic Graphene Films via Laterally Stitched Growth and Structural Repair of Isolated Flakes for Transparent Electronics. *Chem. Mater.* **2017**, *29*, 7808−7815.

(28) Wang, L.; Qiu, H.; Liang, C. B.; Song, P.; Han, Y. X.; Han, Y. X.; Gu, J. W.; Kong, J.; Pan, D.; Guo, Z. H. Electromagnetic Interference Shielding MWCNT-Fe$_3$O$_4$@Ag/Epoxy Nanocomposites with Satisfactory Thermal Conductivity and High Thermal Stability. *Carbon* **2019**, *141*, 506−514.

(29) Liu, J.; Liu, Y. F.; Zhang, H. B.; Dai, Y.; Liu, Z. S.; Yu, Z. Z. Superelastic and Multifunctional Graphene-Based Aerogels by Interfacial Reinforcement with Graphitized Carbon at High Temperatures. *Carbon* **2018**, *132*, 95−103.

(30) Xiao, S.; Yang, Y.; Zhong, M.; Chen, H.; Zhang, Y.; Yang, J.; Zheng, J. Salt-Responsive Bilayer Hydrogels with Pseudo-Double-Network Structure Actuated by Polyelectrolyte and Antipolyelectrolyte Effects. *ACS Appl. Mater. Interfaces* **2017**, *9*, 20843−20851.

(31) Shen, X.; Wang, Z.; Wu, Y.; Liu, X.; Kim, J. K. Effect of Functionalization on Thermal Conductivities of Graphene/Epoxy Composites. *Carbon* **2016**, *108*, 412−422.

(32) Fang, H.; Zhao, Y.; Zhang, Y.; Ren, Y.; Baio, S.-L. Three-Dimensional Graphene Foam-Filled Elastomer Composites with High Thermal and Mechanical Properties. *ACS Appl. Mater. Interfaces* **2017**, *9*, 26447−26459.

(33) Song, J.; Chen, C.; Zhang, Y. High Thermal Conductivity and Stretchability of Layer-by-Layer Assembled Silicone Rubber/Graphene Nanosheets Multilayered Films. *Composites, Part A* **2018**, *105*, 1−8.

(34) Zhang, X.; Zheng, J.; Fang, H. M.; Zhang, Y. F.; Bai, S. L.; He, G. S. Al$_2$O$_3$/Graphene Reinforced Bio-Inspired Interlocking Polyurethane Composites with Superior Mechanical and Thermal Properties for Solid Propulsion Fuel. *Compos. Sci. Technol.* **2018**, *167*, 42−52.

(35) Qin, M.; Xu, Y.; Cao, R.; Feng, W.; Chen, L. Efficiently Controlling the 3D Thermal Conductivity of a Polymer Nanocomposite via a Hyperelastic Double-Continuous Network of Graphene and Sponge. *Adv. Funct. Mater.* **2018**, *28*, No. 1805053.

(36) Guo, Y.; Ruan, K.; Yang, X.; Ma, T.; Kong, J.; Wu, N.; Zhang, J.; Gu, J.; Guo, Z. Constructing Fully Carbon-Based Fillers with A Hierarchical Structure to Fabricate Highly Thermally Conductive Polyimide Nanocomposites. *J. Mater. Chem. C* **2019**, *7*, 7035−7044.

(37) Xiao, S.; Zhang, M.; He, X.; Huang, L.; Zhang, Y.; Ren, B.; Zhong, M.; Chang, Y.; Yang, J.; Zheng, J. Dual Salt-and Thermores-

ponsive Programmable Bilayer Hydrogel Actuators with Pseudo-Interpenetrating Double-Network Structures. *ACS Appl. Mater. Interfaces* **2018**, *10*, 21642−21653.

(38) Huangfu, Y.; Liang, C.; Han, Y.; Qiu, H.; Song, P.; Wang, L.; Kong, J.; Gu, J. Fabrication and Investigation on the Fe₃O₄/thermally Annealed Graphene Aerogel/epoxy Electromagnetic Interference Shielding Nanocomposites. *Compos. Sci. Technol.* **2019**, *169*, 70−75.

(39) Si, Y.; Samulski, E. T. Exfoliated Graphene Separated by Platinum Nanoparticles. *Chem. Mater.* **2008**, *20*, 6792−6797.

(40) Tan, H. L.; Du, A. J.; Amal, R.; Ng, Y. H. Decorating Platinum on Nitrogen-Doped Graphene Sheets: Control of the Platinum Particle Size Distribution for Improved Photocatalytic H₂ Generation. *Chem. Eng. Sci.* **2019**, *194*, 85−93.

(41) Shabnam, L.; Faisal, S. N.; Roy, A. K.; Gomes, V. G. Nickel-Nanoparticles on Doped Graphene: A Highly Active Electrocatalyst for Alcohol and Carbohydrate Electrooxidation for Energy Production. *ChemElectroChem* **2018**, *5*, 3799−3808.

(42) Zhang, J.; Kong, Q.; Wang, D. Simultaneously Improving the Fire Safety and Mechanical Properties of Epoxy Resin with Fe-CNTs via Large-Scale Preparation. *J. Mater. Chem. A* **2018**, *6*, 6376−6386.

(43) Amoli, B. M.; Trinidad, J.; Hu, A.; Zhou, Y. N.; Zhao, B. Highly Electrically Conductive Adhesives Using Silver Nanoparticle (Ag NP)-Decorated Hraphene: the Effect of NPs Sintering on the Electrical Conductivity Improvement. *J. Mater. Sci.: Mater. Electron.* **2015**, *26*, 590−600.

(44) Fan, Z. J.; Liu, B.; Wang, J. Q.; Zhang, S. Y.; Lin, Q. Q.; Gong, P. W.; Ma, L. M.; Yang, S. R. A Novel Wound Dressing Based on Ag/Graphene Polymer Hydrogel: Effectively Kill Bacteria and Accelerate Wound Healing. *Adv. Funct. Mater.* **2014**, *24*, 3933−3943.

(45) Zhu, C.; Guo, S.; Fang, Y.; Dong, S. Reducing Sugar: New Functional Molecules for the Green Synthesis of Graphene Nano-sheets. *ACS Nano* **2010**, *4*, 2429−2437.

(46) Huang, J. R.; Zhu, Y. T.; Xu, L. N.; Chen, J. W.; Jiang, W.; Nie, X. A. Massive Enhancement in the Thermal Conductivity of Polymer Composites by Trapping Graphene at the Interface of A Polymer Blend. *Compos. Sci. Technol.* **2016**, *129*, 160−165.

(47) Wang, F.; Yao, Y.; Zeng, X.; Huang, T.; Sun, R.; Xu, J.; Wong, C. P. Highly Thermally Conductive Polymer Nanocomposites Based on Boron Nitride Nanosheets Decorated with Silver Nanoparticles. *RSC Adv.* **2016**, *6*, 41630−41636.

(48) Chen, Y. P.; Hou, X.; Kang, R. Y.; Liang, Y.; Guo, L. C.; Dai, W.; Nishimura, K.; Lin, C. T.; Jiang, N.; Yu, J. H. Highly Flexible Biodegradable Cellulose Nanofiber/Graphene Heat-Spreader Films with Improved Mechanical Properties and Enhanced Thermal Conductivity. *J. Mater. Chem. C* **2018**, *6*, 12739−12745.

(49) Cheng, C. B.; Fan, R. H.; Wang, Z. Y.; Xie, P. T.; Hou, C. X.; Fan, G. H.; Lei, Y. H.; An, L. Q.; Liu, Y. Radio-Frequency Negative Permittivity in the Graphene/Silicon Nitride Composites Prepared by Spark Plasma Sintering. *J. Am. Ceram. Soc.* **2018**, *101*, 1598−1606.

(50) Zhao, J.; Sun, M.; Liu, Z.; Quan, B.; Gu, C.; Li, J. Three Dimensional Hybrids of Vertical Graphene-Nanosheet Sandwiched by Ag-Nanoparticles for Enhanced Surface Selectively Catalytic Reactions. *Sci. Rep.* **2015**, *5*, No. 16019.

(51) Romeo, V.; Gorrasi, G.; Vittoria, V.; Chronakis, I. S. Encapsulation and Exfoliation of Inorganic Lamellar Fillers into Polycaprolactone by Electrospinning. *Biomacromolecules* **2007**, *8*, 3147−3152.

(52) Mit-uppatham, C.; Nithitanakul, M.; Supaphol, P. Ultratine Electrospun Polyamide-6 Fibers: Effect of Solution Conditions on Morphology and Average Fiber Diameter. *Macromol. Chem. Phys.* **2004**, *205*, 2327−2338.

(53) Chen, L. F.; Zhao, P. F.; Xie, H. Q.; Yu, W. Thermal Properties of Epoxy Resin Based Thermal Interfacial Materials by Filling Ag Nanoparticle-Decorated Graphene Nanosheets. *Compos. Sci. Technol.* **2016**, *125*, 17−21.

(54) Rivière, L.; Lonjon, A.; Dantras, E.; Lacabanne, C.; Olivier, P.; Gleizes, N. R. Silver Fillers Aspect Ratio Influence on Electrical and Thermal Conductivity in PEEK/Ag Nanocomposites. *Eur. Polym. J.* **2016**, *85*, 115−125.

(55) Zhang, L.; Li, X. Y.; Deng, H.; Jing, Y.; Fu, Q. Enhanced Thermal Conductivity and Electrical Insulation Properties of Polymer Composites via Constructing Pglass/CNTs Confined Hybrid Fillers. *Composites, Part A* **2018**, *115*, 1−7.

(56) Liu, S. Q.; Zhao, B.; Jiang, L.; Zhu, Y. W.; Fu, X. Z.; Sun, R.; Xu, J. B.; Wong, C. P. Core-Shell Cu@rGO Hybrids Filled in Epoxy Composites with High Thermal Conduction. *J. Mater. Chem. C* **2018**, *6*, 257−265.

(57) Huang, L.; Zhu, P. L.; Li, G.; Lu, D. Q.; Sun, R.; Wong, C. P. Core-Shell SiO₂@RGO Hybrids for Epoxy Composites with Low Percolation Threshold and Enhanced Thermo-Mechanical Properties. *J. Mater. Chem. A* **2014**, *2*, 18246−18255.

(58) Huang, T.; Zeng, X. L.; Yao, Y. M.; Sun, R.; Meng, F. L.; Xu, J. B.; Wong, C. P. Boron Nitride@Graphene Oxide Hybrids for Epoxy Composites with Enhanced Thermal Conductivity. *RSC Adv.* **2016**, *6*, 35847−35854.

(59) Cecen, V.; Thomann, R.; Muhaupt, R.; Friedrich, C. Thermal Conductivity, Morphology and Mechanical Properties for Thermally Reduced Graphite Oxide-Filled Ethylene Vinylacetate Copolymers. *Polymer* **2017**, *132*, 294−305.

(60) Kim, H. S.; Bae, H. S.; Yu, J.; Kim, S. Y. Thermal Conductivity of Polymer Composites with the Geometrical Characteristics of Graphene Nanoplatelets. *Sci. Rep.* **2016**, *6*, No. 26825.

(61) Qi, G. Q.; Yang, J.; Bao, R. Y.; Xia, D. Y.; Cao, M.; Yang, W.; Yang, M. B.; Wei, D. C. Hierarchical Graphene Foam-Based Phase Change Materials with Enhanced Thermal Conductivity and Shape Stability for Efficient Solar-to-Thermal Energy Conversion and Storage. *Nano Res.* **2017**, *10*, 802−813.

(62) Ji, T. X.; Feng, Y. Y.; Qin, M. M.; Feng, W. Thermal Conducting Properties of Aligned Carbon Nanotubes and Their Polymer Composites. *Composites, Part A* **2016**, *91*, 351−369.

(63) Wang, Z. G.; Huang, Y. F.; Zhang, G. Q.; Wang, H. Q.; Xu, J. Z.; Lei, J.; Zhu, L.; Gong, F.; Li, Z. M. Enhanced Thermal Conductivity of Segregated Poly(vinylidene fluoride) Composites via Forming Hybrid Conductive Network of Boron Nitride and Carbon Nanotubes. *Ind. Eng. Chem. Res.* **2018**, *57*, 10391−10397.

(64) Tang, L.; Dang, J.; He, M. K.; Li, J. Y.; Kong, J.; Tang, Y. S.; Gu, J. W. Preparation and Properties of Cyanate-Based Wave-Transparent Laminated Composites Reinforced by Dopamine/POSS Function-alized Kevlar Cloth. *Compos. Sci. Technol.* **2019**, *169*, 120−126.

(65) Yang, H. L.; Li, Z. L.; Zou, H. W.; Liu, P. B. Preparation of Porous Polyimide/in-situ Reduced Graphene Oxide Composite Films for Electromagnetic Interference Shielding. *Polym. Adv. Technol.* **2017**, *28*, 233−242.

(66) Feng, C. P.; Bai, L.; Bao, R. Y.; Liu, Z. Y.; Yang, M. B.; Chen, J.; Yang, W. Electrically Insulating POE/BN Elastomeric Composites with High Through-Plane Thermal Conductivity Fabricated by Two-Roll Milling and Hot Compression. *Adv. Compos. Hybrid Mater.* **2018**, *1*, 160−167.

(67) Hu, Z. R.; Tong, G. Q.; Nian, Q.; Xu, R.; Saei, M.; Chen, F.; Chen, C. J.; Zhang, M.; Guo, H. F.; Xu, J. L. Laser Sintered Single Layer Graphene Oxide Reinforced Titanium Matrix Nanocomposites. *Composites, Part B* **2016**, *93*, 352−359.